HiSST: 2nd International Conference on
High-Speed Vehicle Science & Technology
11–15 September 2022, Bruges, Belgium

Surface Properties on Fibrous Microstructure for Stardust Re-entry

Michael Kroells[1], *Sahadeo Ramjatan*[2], *Thomas E. Schwartzentruber* [3]

Abstract

New planetary missions will require higher reliability ablative thermal protection systems to handle high heating rates and shear loads while providing the necessary protection for the interior of the vehicle. During the ablation process, thermal stresses and traction forces, combined with oxidation, could affect the structural integrity of individual fibers in the TPS, resulting in failure. This work consists of using the DSMC method to simulate boundary layer flows over resolved fiber microstructures at flight relevant conditions; the necessary boundary conditions for the DSMC simulation are provided using CFD performed on the Stardust capsule. Surface properties including heat flux, traction, and oxygen number flux will be determined on individual fibers, which can be used in a thermal-structural response.

Keywords: *Thermal protection system, DSMC, hypersonics, boundary layer*

1. Introduction

In many atmospheric re-entry missions, ablative carbon-based thermal protection systems (TPS) are used to mitigate vehicle heating. This class of materials, especially Phenolic Impregnated Carbon Ablators (PICA), have been successful on previous missions. PICA consists of a fibrous substrate that is impregnated with phenolic resin. Although PICA has previously been shown to be effective, future missions have higher requirements on reliability; for example, the Mars Sample Return (MSR) mission has very strict reliability requirement to minimize the risk of contaminating the terrestrial environment [1]. To ensure that current and future TPS materials can meet these strict requirements, a better understanding of how these materials interact with a flow field is necessary.

The current work aims to provide a methodology for evaluating the thermo-structural response of a fibrous TPS to a hypersonic boundary layer. Overall, this research is split into 2 parts: using the direct simulation Monte Carlo method (DSMC) to impose a desired boundary layer over a representative fiber bundle and then to use the resulting stresses and heat fluxes on the fibers to perform a thermo-structural material response analysis, which will give insight into the failure modes of the individual fibers. The work in this paper will exclusively focus on the first part of the stated research goals, while the themo-structural response is being performed by our collaborators at the University of Kentucky. [2] In addition to determining the response of the fibrous material to the thermo-structural loads to the enivronment, the resolution of the mesostructure results in realisitc distributions of surface properties, which can be used as an input to probabilitistic modeling of materials [3, 4].

2. Methodology

Our current investigation requires two main components to work effectively: a realistic mesoscale representation of a fibrous PICA-like material and carefully imposed boundary conditions in DSMC for the fluid boundary layer and sub-surface boundaries. This section summarizes the necessary tools and methodologies used for the current work.

[1] *Graduate Research Assistant, Aerospace Engineering and Mechanics, University of Minnesota, kroel012@umn.edu*

[2] *Graduate Research Assistant, Aerospace Engineering and Mechanics, University of Minnesota, ramja003@umn.edu@umn.edu*

[3] *Professor, Aerospace Engineering and Mechanics, University of Minnesota, schwartz@umn.edu*

2.1. Mesoscale fiber bundle generation

In the current work, the mesoscale was generated with the intention to match PICA as much as possible. PICA uses Fiberform ®(Fiber Materials, Inc.), a rigid carbon fiber composite as a substrate that consists of thin carbon fibers (≈10 µm in diameter) and pores of 50 µm in diameter and a high porosity ($\epsilon > 0.85$) [5]. Due to its manufacturing method, Fiberform is tranverse isotropic since most of the fibers are aligned within $\pm$15° of the compression plane [6]. To create an artificially generated fiber bundle that closely resembles PICA, the authors use the FiberGen code developed at the University of Minnesota [7, 8]. FiberGen randomly generates cylinders using triangular surface elements in a specified volume, where the radius, orientation and length of the fibers can be fixed or set from some distribution. A fiber bundle of nominal dimensions (x-y-z) 1.0 mm $\times$ 0.2 mm $\times$ 0.2 mm was formed using FiberGen, with a target porosity of 0.85 and a fiber diameter of 10 µm . This bundle can be found in Fig. 1 and is used in all simulations for the current work in order to generate consistent results.

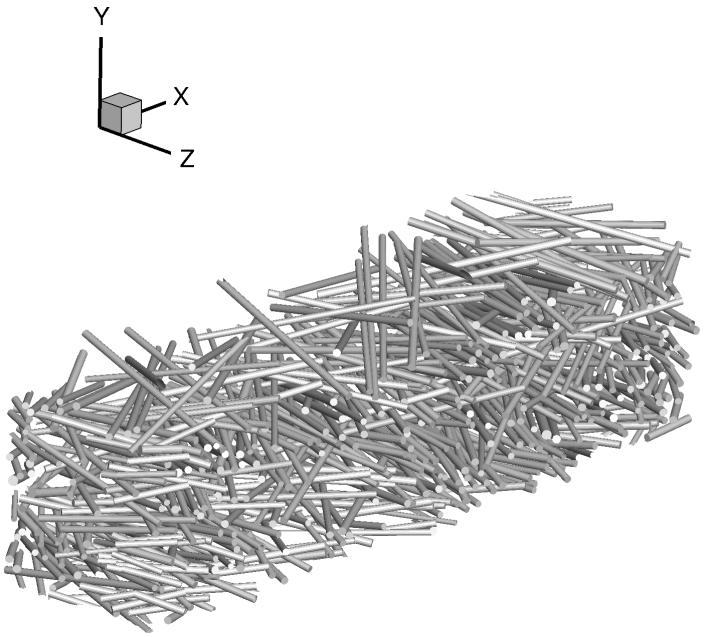

Fig 1. Fiber bundle generated using FiberGen.

2.2. Extracting boundary layers from CFD solutions

In this work, CFD data is taken from a Stardust trajectory simulation with a non-catalytic wall boundary condition [9]. In order to avoid wall curvature effects, data is extracted from the straight portion of the capsule; Figure 2 illustrates the location and procedure for boundary layer extraction. Care must be taken to ensure that the extracted profile is actually normal to the wall, as even a small misalignment will result in an unrealistic boundary layer. This is a result of the high-speed nature of the flow; the wall tangential velocity is much faster than the wall normal velocity and therefore incorrect rotations will result in significantly erroneous wall normal velocities.

2.3. Imposing Chapman-Enskog distributions for multi-component gas

Normally in a hypersonic DSMC simulation, sampling from a Maxwellian (equilibrium) velocity distribution function (VDF) is sufficient to impose boundary conditions on a simulation. By definition, the free stream ahead of the body of interest in a supersonic flow is unaffected by the presence of the body, so the free-stream conditions can usually be set by sampling from a Maxwellian VDF. However, the objective is to extract a boundary layer from an existing CFD simulation and impose it on a DSMC domain. Within a

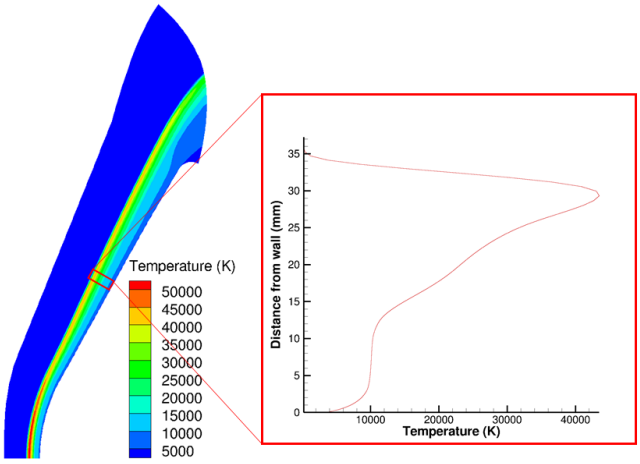

Fig 2. Illustration of extraction of Stardust CFD data in the wall normal direction using temperature as an example.

boundary layer, significant gradients of velocity and temperature exist, which can perturb the VDF of the gas into slight translational non-equilibrium; in fact, this slight translational non-equilibrium corresponds to the viscous terms in the Navier-Stokes equations. While the cases of interest fall within the continuum regime (i.e the Navier-Stokes equations are valid), attempting to sample boundary conditions from Mawellian VDFs results in noticeable errors in the boundary layer profile. In order to resolve this, the imposed VDFs need to be sampled from Chapman-Enskog (C-E) distributions. Most of the details of this procedure are omitted for brevity, but our method uses the efficient algortihm for sampling from a C-E distribution developed by Garcia and Alder [10].

2.4. Boundary conditions

In order to properly simulate a hypersonic boundary layer over the mesostructure, different boundary conditions need to be applied in different regions. Figure 3 shows a 2-D cut of the DSMC domain and gives some insight into how boundary conditions are applied. At the boundaries of the rectangular domain, 3 types of BCs are used; specular reflections, periodic particle movement, and particle deletion. Particles that strike a surface triangle of the fibers are diffusely reflected with full thermal accommodation at the fiber temperature. Particles are only deleted if they cross a deletion boundary from the interior of the domain. Particles moving inside the domain from the ghost region are not deleted. Periodic BCs are a new feature added to MGDS to support this work. While periodic BCs are conceptually simple, their addition in a massively parallel DSMC architecture required significant effort. At the top and bottom of the domain (y-direction), simulated DSMC particles are specularly reflected when they reach the domain boundary. In the x-direction, particles that leave the domain are deleted above the fiber height, but below the fiber height particles that reach the domain boundary are moved to the other size of the domain (x-direction) to the associated periodic location. Particles retain all their properties when moved to the other side of the domain, including their velocity vectors and y and z location. While the fibers themselves are not periodic, the addition of periodic boundary conditions below the fiber surface allows for the flow region within the fibers to develop naturally instead of enforcing an arbitrary gas state. Although not shown in Fig. 3, the boundaries of the domain in the z-direction specularly reflect simulated particles.

In order to enforce the gas state, a variation on the commonly used volumetric reservoir approach is used. Two ”ghost” regions, which have the same y and z sizes as the surface deletion regions on the x faces of the DSMC domain, are used to generate DSMC particles. These particles are sampled from C-E distributions, where the gas state is interpolated linearly from the extracted CFD boundary layer profile. The boundary layer profile starts at the top of the fiber region and data is interpolated from the CFD data

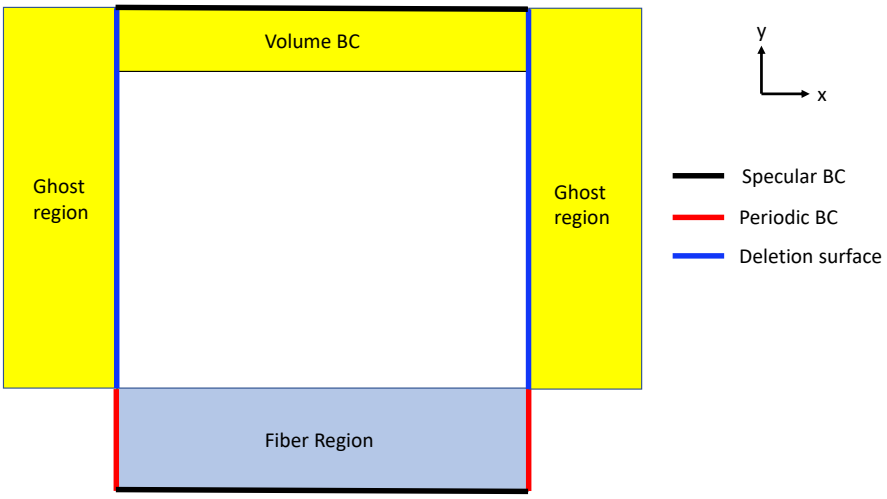

Fig 3. 2-D depiction of DSMC boundary conditions.

based on the distance in the y-direction from the top of the fiber region. Particles are generated within both ghost regions using the volumetric reservoir approach [11]. After the particles are generated, a test is performed on each particle to determine if it will move within the DSMC domain within the current timestep; only the particles that will move within the domain are retained. At the top of the domain (y-direction), there is no interface between periodic and enforced states, so the volumetric reservoir approach is applied. The same method is used to determine the state (interpolation from CFD boundary layer) and sampled from C-E distributions as within the ghost regions.

3. Results/Discussion

3.1. DSMC Setup

We examine the highest (81 km) and lowest (68.9 km) altitude condition simulated by Martin and Boyd [9]. A line of wall normal data was extracted from the location indicated in Fig. 2 for both the high and low altitude cases. The fiber temperature was set to 2650 and 3310 K for the 81 and 68.9 km cases, respectively. These temperatures coorespond to the surface temperatures used in the study of Martin and Boyd. The DSMC domain has the shape of a rectangular prism (not including the ghost regions) with a size that matched the fiber bundle size in the x and z direction (1 mm x 0.2 mm, respectively). In the y direction, the domain includes the height of the fibrous structure (0.2 mm) and an additional 2.8 mm for a total of 3 mm. The DSMC grid is sized to be x0.25 and x0.5 the smallest mean free path in the domain (right above the mesostructure) for 81 and 68.9 km cases, which resulted in a 54,000 and 352,000 total cells, respectively. At least 20 simulated DSMC particles per cell were used everywhere in the domain and in most cells had many more than 20. This resulted in roughly 5 million total particles for the high altitude case and 17 million total particles for the low altitude case. The timestep was set to 1/20 the minimum mean collision time in the domain for both cases. All these DSMC parameters were set conservatively to ensure an accurate simulation. It took roughly 30k timesteps for the low altitude case to reach steady state and 15k timesteps for the high altitude. Sampling of flowfield and surface properties only began after steady state was reached.

The non-catalytic CFD solution used an 11 species air model, however, most of the species were only present in trace amounts in the extracted boundary layer. While the MGDS code has the capability to simulate 11 species air, we decided to reduce the complexity of the problem as much as possible and only kept the major gas components. Neutral and ionized species were lumped together. In our simulations, we only considered N, O, and N_2; at minimum, these components made up 99.98% of the total gas density for the low altitude case and 99.7% for the high altitude case within the simulated

region of the extracted boundary layer.

3.2. Visualization of flowfield and surface properties

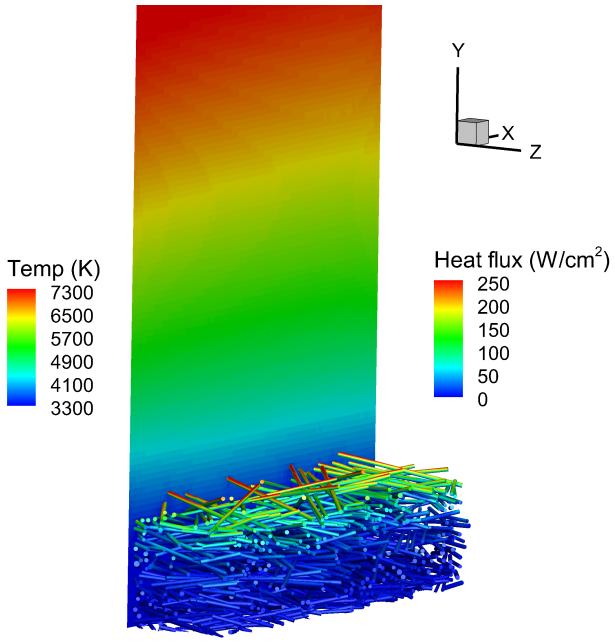

Fig 4. Visualization of heat flux on fiber bundle and temperature field above the bundle for the 68.9 km case.

Figure 4 shows an example visualization of the boundary layer and the fiber bundle for the 68.9 km case. Contours of temperature are shown in the boundary layer slice and heat flux is shown on the fiber bundle. As expected, the heat flux is highest on the fibers nearest to the surface, but the heat flux decreases very rapidly as the depth into the fiber bundle increases. The temperature gradient in the boundary layer is very significant; the temperature jumps from 3310 K at the surface of the fiber bundle to nearly 7500 K within a millimeter of the surface. This extreme boundary layer is the result of the severe entry conditions the Stardust mission experienced. The boundary layer also appears relatively consistent across the fiber bundle in the x-direction.

Figure 5 shows a z-slice of the domain with horizontal velocity contours and streamlines close to the fiber surface, along with fibers triangles close to the z-location of the slice. The boundary layer over the bundle is very smooth away from the surface, but the streamlines begin to bend nearer to the surface. The streamlines are deflected over protrusions of fibers and a small amount of flow is seen through the upper parts of the bundle. The smoothness of the boundary layer and the seamless transition to flow through the bundle is the outcome of the carefully applied boundary conditions and allows for a realistic representation of flow through and into the artificial bundle.

Figure 6 contains comparisons of the heat flux and traction forces on the triangles in the fiber bundle for the two cases considered. Traction forces are defined as the magnitude of the forces perpendicular to the triangle normal direction. These forces are related to the shear stress on each triangle. Figure 6 shows the data on the triangles in the form of probability distribution functions (PDFs) on a log scale. For heat flux, there is a sharp peak for both cases around 0 heating, which corresponds to fibers near the bottom of the bundle. The fibers near the bottom experience essentially no heating as the gas surrounding the fibers is equilibrated at the fiber temperature. The width of this peak is related to the statistics on the triangles; for a finite number of samples and simulated particles, there will be some statistical variation in any sampled quantity. However, this was minimized by using a large number of particles and sampling timesteps, which is why the peak drops off very quickly for negative heat fluxes.

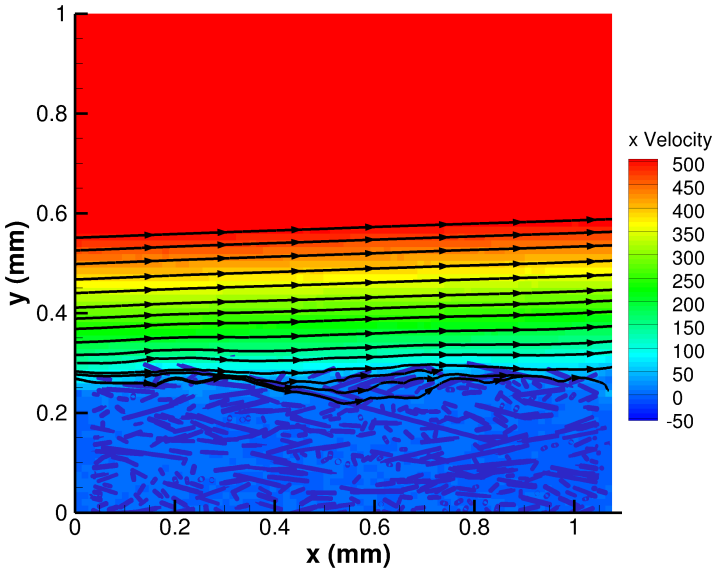

Fig 5. Contours of wall tangential velocity and velocity streamlines near the fiber surface.

In the other direction, the PDF drops off much more gradually and shows a smooth variation from the maximum PDF value to the triangles with the maxiumum heat flux. Similar trends are also present for the traction forces.

As expected, both the maximum heat flux and traction force magnitudes are higher for the lower altitude case, which is consistent with the CFD results. The CFD values of heat flux at the extraction point are also shown in Fig. 6a; there are very few triangles with a heat flux greater than the CFD value. The triangle heat flux values are generally lower on the fibers because the fiber bundle has a larger area to distribute the incoming heat energy as compared to a planar CFD surface cell.

3.3. Comparison of boundary layer with and without C-E boundary conditions

As previously mentioned, the lack of C-E boundary conditions in DSMC simulation can cause significant errors in the flowfield, even when the flow is in the continuum regime. Figure 7 shows a comparison of the wall normal velocity when C-E are included and when Maxwellian VDFs are imposed. Clearly, there is a major difference in the wall normal velocities. The lack of C-E BCs causes a large wall normal velocity (> 100 m/s) away from the fiber bundle across most the domain. The wall normal velocity shows the most difference between the BC methods, but small differences in density, wall tangential velocity, and temperature are also present.

4. Conclusions

In order to better understand the interaction between a a hypersonic flow field and a fibrous mesostructure, the DSMC method was used to impose an extracted CFD Stardust boundary layer over a artificially generated fiber bundle. The fiber bundle consists of cylinders made using the FiberGen code, however, any mesoscale representation that consists of triangular STL surfaces could be used with this method. The imposition of the CFD boundary layer requires carefully considered boundary conditions in DSMC. The original data extraction needs to include gradients of velocity and temperature, as well as per species transport properties (viscosity and thermal conductivity). These variables are needed to sample from Chapman-Enskog distributions, which account for perturbations to the equilibrium Maxwell-Boltmann

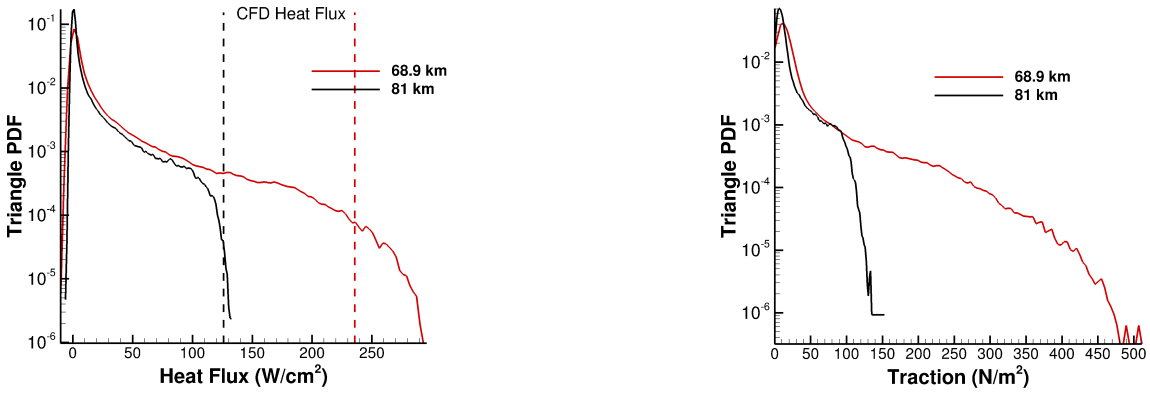

(a) PDF of heat flux

(b) PDF of traction forces

Fig 6. Distributions of surface properties on the triangles that make the fiber bundle for both the 68.9 km and 81 km case. The computed CFD heat flux from Martian and Boyd is also included for the extracted BL location at both conditions.

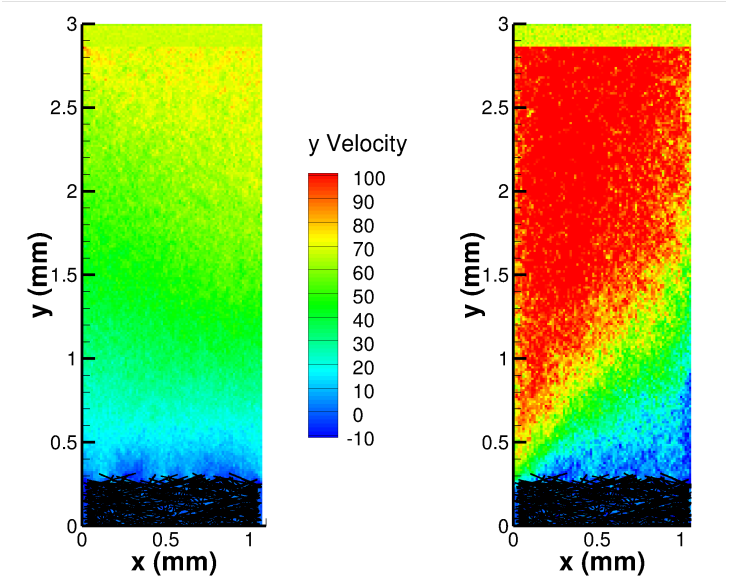

Fig 7. Comparison of wall normal velocity with (left) and without C-E boundary (right) conditions for the 68.9 km case.

distribution that arise from strong molecular transport. A combination of boundary conditions, including C-E particle generation, periodic movement, particle deletion are needed to obtain a high quality representation of the flow over the mesostucture.

Two altitudes (68.9 and 81 km) were considered along the Stardust entry trajectory and surface properties were obtained by sampling over a long time period at a steady-state DSMC solution. Specifically, PDFs of heat flux and traction force were obtained, which have been used as the input to a thermo-structural response and could be used to inform probabilistic modeling of TPS materials. The PDF for heat flux is maximum near 0 W/km^2 and smoothly descreases to a maximum heat flux that is slightly lower than the predicted CFD heat flux. Very few triangles have a heat flux higher than the CFD heat flux because the fibrous mesostructure has a larger surface area than the equivalent CFD surface element. The traction force shows similar trends, but there is no comparison value from the CFD data. In addition to PDFs of surface quantities , some comparisons of the flow field with and without C-E particle generation were shown to highlight their importance.

Acknowledgments

This work was supported by a NASA Space Technology Research Fellowship under grant number 80NSSC19K1129 and by a Space Technology Research Institutes grant from NASA's Space Technology Research Grants Program.

References

[1] Dillman, R. J., and Corliss, J. M., "Overview of the Mars Sample Return Earth Entry Vehicle," *6th International Planetary Probe Workshop*, 2008.

[2] Fu, R., Ramjatan, S., Kroells, M., Schwartzentruber, T., and Martin, A., "Micro-Scale Thermal-Structural Modeling for Carbon Fibers," *AIAA Aviation 2020 Forum*, 2020.

[3] McDaniel, S., Seif, M., Fu, R., Beck, M., and Martin, A., "Development of Stochastic Model for Fibrous Ablators," *AIAA Scitech 2021 Forum*, 2021.

[4] Fu, R., Schmitt, S., and Martin, A., "Thermo-Chemical-Structural Modeling of Carbon Fiber Pitting and Failure Mechanism," *AIAA Scitech 2022 Forum*, 2022.

[5] Lachaud, J., Cozmuta, I., and Mansour, N. N., "Multiscale approach to ablation modeling of phenolic impregnated carbon ablators," *Journal of Spacecraft and Rockets*, Vol. 47, No. 6, 2010, pp. 910–921.

[6] Panerai, F., White, J. D., Cochell, T. J., Schroeder, O. M., Mansour, N. N., Wright, M. J., and Martin, A., "Experimental measurements of the permeability of fibrous carbon at high-temperature," *International Journal of Heat and Mass Transfer*, Vol. 101, 2016, pp. 267–273.

[7] Stern, E. C., Poovathingal, S., Nompelis, I., Schwartzentruber, T. E., and Candler, G. V., "Nonequilibrium flow through porous thermal protection materials, Part I: Numerical methods," *Journal of Computational Physics*, Vol. 380, 2019, pp. 408–426.

[8] Poovathingal, S., Stern, E., Nompelis, I., Schwartzentruber, T., and Candler, G., "Nonequilibrium flow through porous thermal protection materials, Part II: Oxidation and pyrolysis," *Journal of Computational Physics*, Vol. 380, 2019, pp. 427–441.

[9] Martin, A., and Boyd, i., "Modeling of Heat Transfer Attenuation by Ablative Gases During the Stardust Reentry," *Journal of Thermophysics and Heat Transfer*, Vol. 29, 2015. doi:10.2514/1.T4202.

[10] Garcia, A., and Alder, B., "Generation of the Chapman-Enskog Distribution," *Journal of Computational Physics*, Vol. 140, 1998, pp. 66–70.

[11] Tysanner, M. W., and Garcia, A. L., "Non-equilibrium behaviour of equilibrium reservoirs in molecular simulations," *International Journal for Numerical Methods in Fluids*, Vol. 48, No. 12, 2005, pp. 1337–1349.